ELSEVIER

Diamond and Related Materials 9 (2000) 1320–1326

DIAMOND AND RELATED MATERIALS

www.elsevier.com/locate/diamond

Construction of a new C–H–O ternary diagram for diamond deposition from the vapor phase

Sally C. Eaton[1], Mahendra K. Sunkara*

Department of Chemical Engineering, University of Louisville, Louisville, KY 40292, USA

Received 22 September 1999; accepted 27 January 2000

Abstract

A new C–H–O ternary diagram is presented based on radical species composition showing the regions for diamond deposition, non-diamond deposition, and no deposition from the vapor phase. This construction is based on the steady-state computations of gas-phase and gas-surface chemistry from the data points presented in the C–H–O ternary diagram based on feed gas composition by Bachmann et al. (P.K. Bachmann, D. Leers, H. Lydtin. Diamond Relat. Mater. 1 (1991) 1). The analysis of the computational results indicates that the radical species composition does distinguish the three regions and helps explain the contradicting experimental data points using non-typical gas mixtures. The analysis also shows that the revised diagram based on radical species composition works only when carbon monoxide (CO) is treated as a non-participating species. The effects of temperature, pressure and flow rates on this new ternary diagram are also detailed. © 2000 Elsevier Science S.A. All rights reserved.

Keywords: Chemical vapor deposition; Diamond; Radical species; Composition

1. Introduction

The process parametric window for diamond deposition from the vapor phase at low pressures is quite limited. With the addition of oxygen in the gas phase, diamond can be grown within a confined but broader parametric window than with hydrogen and hydrocarbons alone. This is best illustrated in a triangular diagram depicted by Bachmann et al. (Fig. 1) [1]. In this ternary diagram, a narrow region located approximately at the $C/O = 1.0$ line indicates the range of feed gas compositions that result in diamond, non-diamond carbon deposition and no carbon precipitation from the vapor phase as shown in Fig. 1. This depiction is based entirely on various feed gas compositions from 80 experiments on chemical vapor deposition of diamond covering 30 years of research. This diagram was first presented with a wedge-shaped diamond domain and revised to a lens-shaped domain in 1994 [2]. The lower boundary of the lens shaped domain concurs with the H_2–CO tie-line and the upper boundary is parabolic. The diamond domain reduces to a point on the C–O side of the diagram.

By its origin, the Bachmann diagram is limited solely to the determination of feed gas compositions that result in diamond deposition and does not provide any specific information about gas-phase radical compositions that occur in these different regions. Experiments by Marinelli et al. [3] have confirmed the existence of the three regions, but showed that the boundaries of these different regions vary when unconventional feed gases, such as CH_4 and CO_2, are used.

* Corresponding author. Tel.: +1-502-852-6347; fax: +1-502-852-6355.

E-mail address: mahendra@louisville.edu (M.K. Sunkara).

[1] Present address: Department of Chemical Engineering, Case Western Reserve University, Cleveland, OH 44106, USA.

PII: S0925-9635(00)00245-4

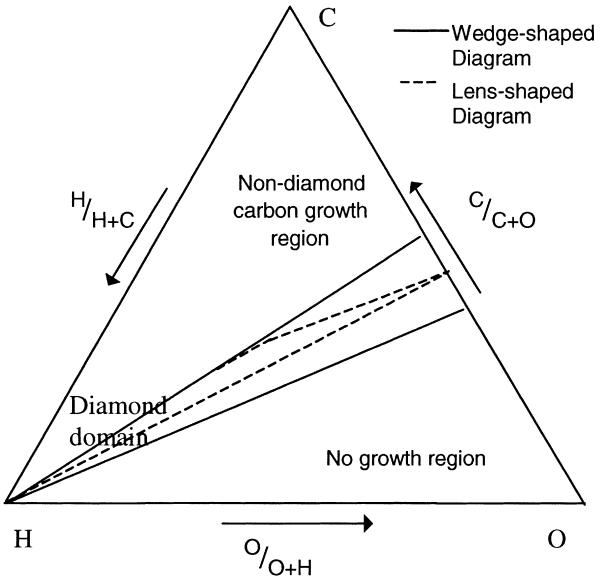

Fig. 1. Original C–H–O ternary phase diagram for diamond deposition from the vapor phase based on feed gas compositions [1].

Prijaya et al. [4] have shown using theoretical considerations that the boundary between the diamond deposition region and the no-growth region is defined by the equilibrium solubility of carbon in the gas phase. Wang et al. [5] developed a non-equilibrium thermodynamic model to justify that the diamond domain reduces to a point on the C–O side of the revised diagram.

Although the Bachmann diagram represents a window of feed gas compositions that yield diamond deposition from the vapor phase, it is not clear whether such a window exists when a radical species composition is considered. If such a domain results from radical species composition, then it would further the use of the Bachmann diagram in analyzing the diamond deposition process onto complicated geometries such as trenches. In addition, it could provide insight into the important radical species that are responsible for diamond growth. Toward this objective, the gas species composition near the gas-diamond interface is critically examined in this paper under steady-state conditions and over a range of C–H–O feed conditions. Specifically, the feed gas compositions in the Bachmann diagram were translated into steady-state species concentrations and were plotted in a triangular C–H–O phase diagram. This was done on the basis that the feed conditions described in the Bachmann diagram produce an essential combination of radicals that will distinguish various regions of carbon deposition from the vapor phase, i.e. diamond deposition, non-deposition and no deposition.

2. Computational procedure

Steady state computations were performed using a zero-dimensional, stirred reactor model with the help of a commercial software package, CHEMKIN III from Reaction Design, Inc., CA. In this program, the gas phase chemistry along with gas-surface chemistry was

Table 1
List of all the elementary reactions used in the model

Gas-phase reactions considered	$A(\frac{cm^3}{mol})^n/s$	b	E(cal/mol)
1. $H + H + M = H_2 + M$	1.00×10^{18}	−1.0	0.0
2. $H + H + H_2 = 2H_2$	9.20×10^{16}	−0.6	0.0
3. $H + H + H_2O = H_2 + H_2O$	6.00×10^{19}	−1.2	0.0
4. $H + H + CO_2 = H_2 + CO_2$	5.49×10^{20}	−2.0	0.0
5. $O + OH = O_2 + H$	4.00×10^{14}	−0.5	0.0
6. $O + H_2 = OH + H$	5.06×10^{4}	2.7	6290.0
7. $2OH = O + H_2O$	1.50×10^{9}	1.1	99.0
8. $2O + M = O_2 + M$	1.20×10^{17}	−1.0	0.0
9. $H_2 + O_2 = 2OH$	1.70×10^{13}	0.0	47 780.0
10. $OH + H_2 = H_2O + H$	1.17×10^{09}	1.3	3626.0
11. $CH_4 + O = CH_3 + OH$	1.02×10^{9}	1.5	8604.0
12. $CH_4 + H = CH_3 + H_2$	1.32×10^{4}	3.0	8040.0
13. $CH_4 + OH = CH_3 + H_2O$	1.60×10^{6}	2.1	2460.0
14. $CH_4 + O_2 = CH_3 + HO_2$	7.90×10^{13}	0.0	56 000.0
15. $CH_4 + HO_2 = CH_3 + H_2O_2$	1.13×10^{13}	0.0	24 641.0
16. $CH_3 + H = CH_2 + H_2$	9.00×10^{13}	0.0	15 100.0
17. $CH_3 + O = CH_2O + H$	8.00×10^{13}	0.0	0.0
18. $CH_3 + OH = CH_2 + H_2O$	7.50×10^{6}	2.0	5000.0
19. $CH_3 + OH = CH_3O + H$	5.74×10^{12}	−0.2	13 931.0
20. $CH_3 + O_2 = CH_3O + O$	2.05×10^{18}	−1.6	29 229.0
21. $CH_3 + O_2 = CH_2O + OH$	3.59×10^{9}	−0.1	10 150.0
22. $CH_3 + HO_2 = CH_3O + OH$	2.00×10^{13}	0.0	0.0
23. $CH_3 + CH_3 = C_2H_4 + H_2$	1.00×10^{16}	0.0	32 005.0
24. $CH_2 + OH = CH_2O + H$	2.50×10^{13}	0.0	0.0
25. $CH_2 + O = CO + 2H$	5.00×10^{13}	0.0	0.0
26. $CH_2 + CO_2 = CH_2O + CO$	1.10×10^{11}	0.0	1000.0
27. $CH_2 + O = CO + H_2$	3.00×10^{13}	0.0	0.0
28. $CH_2 + O_2 = CO_2 + 2H$	1.60×10^{12}	0.0	1000.0
29. $CH_2 + O_2 = CH_2O + O$	2.00×10^{14}	0.0	10 000.0
30. $CH_2 + O_2 = CO_2 + H_2$	6.90×10^{11}	0.0	500.0
31. $CH_2 + O_2 = CO + H_2O$	1.90×10^{10}	0.0	−1000.0
32. $CH_2 + O_2 = CO + OH + H$	8.60×10^{10}	0.0	−500.0
33. $CH_2 + O_2 = HCO + OH$	4.30×10^{10}	0.0	−500.0
34. $CH_2 + CH_3 = C_2H_4 + H$	3.00×10^{13}	0.0	0.0
35. $2CH_2 = C_2H_2 + H_2$	4.00×10^{13}	0.0	0.0
36. $CH_2 + HO_2 = CH_2O + OH$	3.01×10^{13}	0.0	0.0
37. $CH_2 + H_2O_2 = CH_3O + OH$	3.01×10^{13}	0.0	0.0
38. $CH_2 + CH_2O = CH_3 + HCO$	1.20×10^{12}	0.0	0.0
39. $CH_2 + HCO = CH_3 + CO$	1.81×10^{13}	0.0	0.0
40. $CH_2 + H = CH + H_2$	1.00×10^{18}	−1.6	0.0
41. $CH_2 + OH = CH + H_2O$	1.13×10^{7}	2.0	3000.0
42. $CH + O_2 = HCO + O$	3.30×10^{13}	0.0	0.0
43. $CH + O = CO + H$	5.70×10^{13}	0.0	0.0
44. $H + CH = C + H_2$	1.10×10^{14}	0.0	0.0
45. $CH + OH = HCO + H$	3.00×10^{13}	0.0	0.0
46. $CH + CO_2 = HCO + CO$	3.40×10^{12}	0.0	690.0
47. $CH + H_2O = CH_2O + H$	1.17×10^{15}	−0.8	0.0
48. $CH + CH_2O = CH_2CO + H$	9.46×10^{13}	0.0	−515.0
49. $CH + CH_2 = C_2H_2 + H$	4.00×10^{13}	0.0	0.0
50. $CH + CH_3 = C_2H_3 + H$	3.00×10^{13}	0.0	0.0
51. $CH + CH_4 = C_2H_4 + H$	6.00×10^{13}	0.0	0.0
52. $C_2H_3 + CH = CH_2 + C_2H_2$	5.00×10^{13}	0.0	0.0
53. $HCCO + CH = C_2H_2 + CO$	5.00×10^{13}	0.0	0.0
54. $CH + CO(+M) = HCCO (+M)$	5.00×10^{13}	0.0	0.0

Table 1 (*Continued*)

Gas-phase reactions considered	A	b	E
55. OH + C = H + CO	5.00×10^{13}	0.0	0.0
56. C + O_2 = O + CO	5.80×10^{13}	0.0	575.0
57. C + CH_2 = H + C_2H	5.00×10^{13}	0.0	0.0
58. C + CH_3 = H + C_2H_2	5.00×10^{13}	0.0	0.0
59. HCO + M = CO + H + M	2.50×10^{14}	0.0	16 802.0
60. HCO + H = CO + H_2	1.19×10^{13}	0.2	0.0
61. HCO + O = CO + OH	3.00×10^{13}	0.0	0.0
62. HCO + O = CO_2 + H	3.00×10^{13}	0.0	0.0
63. HCO + OH = CO + H_2O	1.00×10^{14}	0.0	0.0
64. HCO + O_2 = CO + HO_2	7.60×10^{12}	0.0	400.0
65. CH_3 + HCO = CH_4 + CO	1.20×10^{14}	0.0	0.0
66. O + CO + M = CO_2 + M	6.17×10^{14}	0.0	3000.0
67. CO + OH = CO_2 + H	1.51×10^{7}	1.3	−758.0
68. O_2 + CO = O + CO_2	2.50×10^{12}	0.0	47 800.0
69. CO + HO_2 = CO_2 + OH	5.80×10^{13}	0.0	22 934.0
70. C_2H_2 + H = C_2H + H_2	6.02×10^{13}	0.0	22 243.0
71. C_2H + O = CH + CO	1.81×10^{13}	0.0	0.0
Surface reactions considered			
1. CH(S) + H → C(S) + H_2	1.30×10^{14}	0.0	7300.0
2. C(S) + H_2 → CH(S) + H	6.50×10^{13}	0.0	7300.0
3. C(S) + H → CH(S)	1.00×10^{13}	0.0	0.0
4. CH(S) → C(S) + H	3.30×10^{12}	0.0	0.0
5. C(S) + CH_3 → CCH_3(S)	5.00×10^{12}	0.0	0.0
6. CCH_3(S) → C(S) + CH_3	1.00×10^{13}	0.0	0.0
7. C(S) + C_2H_2 → CC_2H_2(S)	8.00×10^{10}	0.0	7700.0
8. CC_2H_2(S) → C(S) + C_2H_2	3.20×10^{11}	0.0	7700.0
9. CCH_3(S) + H → CCH_2(S) + H_2	2.80×10^{7}	0.0	7700.0
10. CCH_2(S) + H_2 → CCH_3(S) + H	1.40×10^{7}	0.0	7700.0
11. CCH_2(S) + H → CCH_3(S)	1.00×10^{13}	0.0	0.0
12. CCH_3(S) → CCH_2(S) + H	3.30×10^{12}	0.0	0.0

modeled as a CSTR reactor. The detailed reaction model set included a compilation of 71 elementary gas-phase reactions [6,7] and 12 gas-surface reactions [8] as shown in Table 1. As seen from Table 1, the model set is useful only for feed gases involving methane, hydrogen, oxygen, water, carbon monoxide, and carbon dioxide. Steady state computations using CHEMKIN II without surface chemistry have been used before to study the effects of flow rates on radical species composition [9]. CHEMKIN solves the following steady state mass and mole balance equations for the species considered in the model.

$$\frac{d(\rho V)}{dt} = 0 = \dot{m}_{\text{in}} - \dot{m}_{\text{out}} + A_m \Sigma \dot{s}_k \tag{1}$$

where, ρ is the mass density; V is the volume of the reactor; $\dot{m}_{\text{in}}$ and $\dot{m}_{\text{out}}$ are in the inlet and outlet flow rates, respectively; A is the surface area, and $\Sigma \dot{s}_k$ is the net surface production rate over all components.

The steady-state mass balance of each gas-phase component is given by Eq. (2) below:

$$\frac{\mathrm{d}X_k}{\mathrm{d}t} = 0 = \frac{\dot{m}_{\text{in}}}{\rho V}(X_{k,\text{in}} - X_{k,\text{out}}) + \dot{w}_k + \frac{A\dot{s}_k}{\rho V} \tag{2}$$

where X_k is the mass fraction of component k and w_k is the net gas-phase production rate.

As seen from the above, no transport effects were included in the stirred tank model. However, the effect of flow rate was included. The following 26 species were considered in the model: O_2, H_2O, H_2O_2, H, O, OH, HO_2, CH_2CO, C, H_2, CH_3O, HCO, C_2H_2, C_2H_3, C_2H_4, HCCO, C_2H_6, CH_4, CH_3, CH_2, CH, C_2H, CH_2, CO_2, CO and CH_2O. Typical process conditions for the computations were 1150 K for temperature, 50 torr for pressure, and 200 sccm for flow rate unless specified. Because of the CSTR model, the bulk gas phase temperature was the same as the growth interface temperature. Discrete feed gas compositions were selected from the three regions in the Bachmann diagram that are possible with methane, hydrogen and oxygen as feed gases. The resulting steady-state composition of important radical species compare well with the published values in literature [10,11] for similar process conditions thus validating the chosen reaction set.

3. Results

The steady-state computational results were analyzed by dividing the species into two categories: 'non-participating' and 'participating' species. The compounds CH_4, O_2, H_2, H_2O, CO and CO_2 were considered as non-participating species. Various combinations of 'non-participating' species were considered in constructing the ternary diagram. For the remaining 'participating' species, the total elemental mole fractions of H, C, and O were calculated. The data points were generated with various feed gas compositions taken from the entire spectrum of possible feed compositions using H_2, O_2, and CH_4 as gases.

The resulting radical species compositions were first analyzed by including carbon monoxide among the participating species. However, the inclusion of CO failed to distinguish steady state, gas phase compositional regions for diamond deposition, no-deposition, and non-diamond deposition. The resulting diagram provided no meaningful, practical information into the gas-phase mixtures influencing each of the three growth regimes. The choice of participating species obviously affects the resulting diagram. Therefore, several choices for non-participating species were investigated.

Fig. 2 shows the resulting in-situ diagram when CO was not included as a participating species. This new C–H–O ternary diagram clearly distinguishes the three regions during diamond deposition from the vapor phase and is also consistent with the Bachmann diagram. A C–H–O ternary phase diagram based on radical species resulted when CO was treated as a non-participating species. This result confirms earlier hypothe-

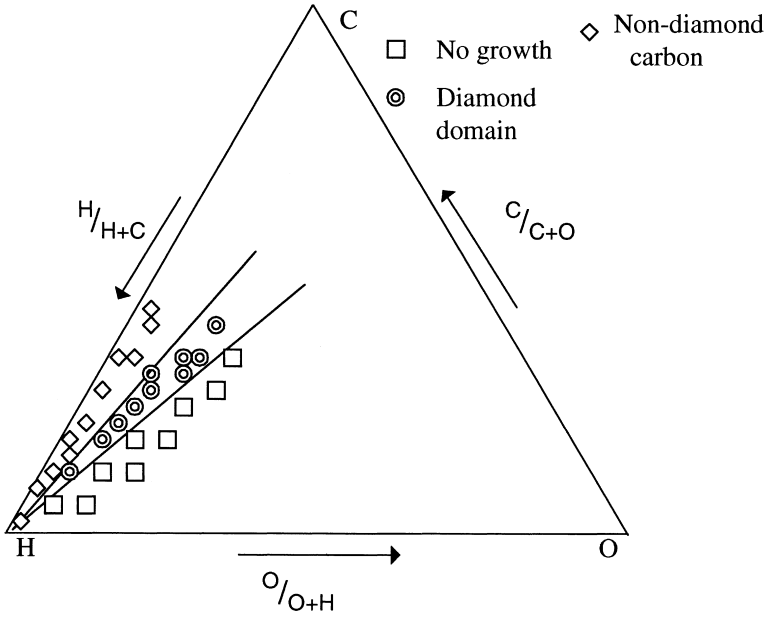

Fig. 2. The new C–H–O ternary phase diagram based on radical species composition showing the different regions for diamond deposition, non-diamond deposition and no deposition from the vapor deposition. The pressure was 50 torr and temperature was 1150 K.

ses that the stability of CO in the gas phase rationalizes the existence of three regions in the Bachmann diagram [4,12,13].

The inclusion of molecular oxygen as a participating species had a negligible effect on the boundaries of the resulting in-situ diagram. On the other hand, the inclusion of carbon dioxide and water as participating species shifts the boundary lines closer to the oxygen vertex. This in-situ diagram is not shown in this paper. However, these species (CH_4, CO_2 and H_2O) were considered as non-participatory due to their minimal effect on the known gas-surface chemistry.

The new in-situ diagram was tested for its accuracy with the data points from the lens-shaped Bachmann diagram using feed compositions along the CH_4/CO tie-line and the CO/H_2 tie-line (Fig. 3). The selected data points located on the CH_4/CO tie-line were within the diamond domain in the wedge type diagram and within the non-diamond region according to the lens shaped diagram. On the in-situ C–H–O ternary diagram, these data points fell within non-diamond deposition region consistent with the lens-shaped Bachmann diagram. The second set of selected data points located along the CO/H_2 tie-line were within the diamond deposition domain according to both versions of the Bachmann diagrams. On the in-situ C–H–O ternary diagram, these data points fell at the hydrogen vertex and well inside the diamond deposition domain. These results suggest that the boundaries of the in-situ diagram shown in Fig. 2 can be extended linearly. Extensive testing using the feed gas compositions from region close to C–O side of the ternary diagram is essential to determine the nature of upper and lower

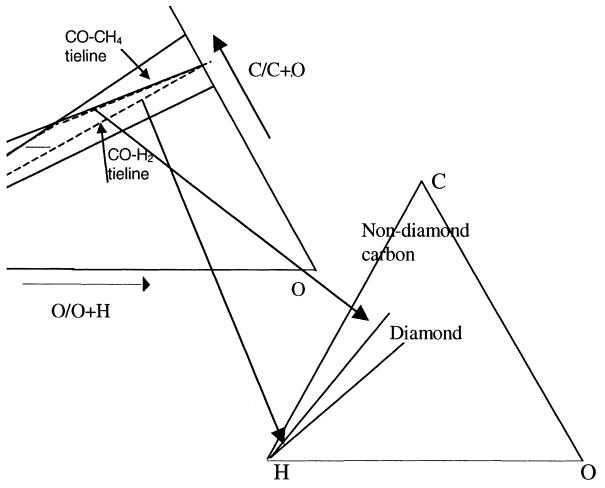

Fig. 3. Feed conditions with CH_4/CO and CO/H_2 and the resulting radical species concentrations.

boundary lines in the in-situ diagram close to C–O line. It is also possible that the upper and lower boundary lines never intersect the C–O side of the ternary diagram because CO is treated as non-participatory.

The validity of the in-situ C–H–O diagram in Fig. 2 was also tested using different combinations of feed gases such as hydrogen, methane, water and carbon monoxide. Fig. 4 shows the resulting diagram with alternate feed gases and is found to be identical to that obtained in Fig. 2 using methane, hydrogen and oxygen as feed gases.

The feed conditions of Marinelli et al. [3] using methane and carbon dioxide were also modeled. They

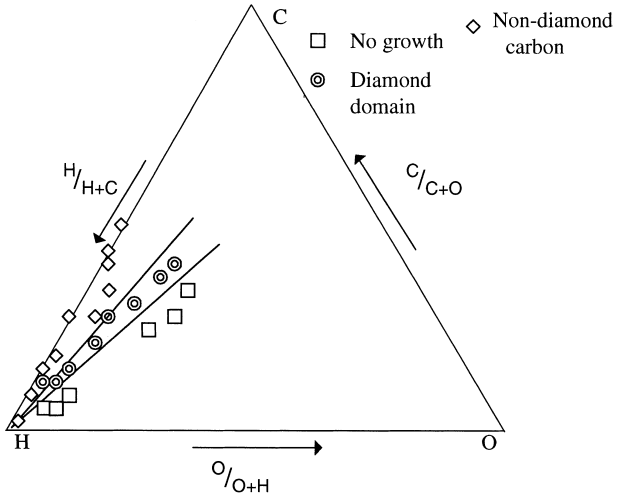

Fig. 4. The effect of different gas mixtures on the new C–H–O ternary phase diagram based on radical species composition for vapor deposition of diamond. Various mixtures of H_2, CH_4, H_2O and CO were used as feed gases at 50 torr and 1150 K.

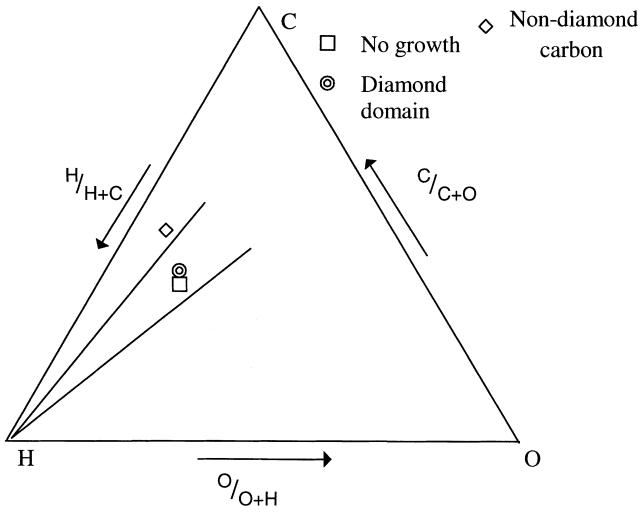

Fig. 5. The resulting data points corresponding to experimental feed conditions by Marinelli et al [3]. on the new, C–H–O ternary diagram based on radical species composition.

used feed gases of methane and carbon dioxide and their samples showed that non-diamond carbon and no growth could occur in the traditional diamond-growing domain of the Bachmann diagram. It is hypothesized here that although the feed conditions did not agree with the Bachmann diagram, that the resulting radical species composition would agree with our new in-situ C–H–O diagram in Fig. 2. The results of their experimental conditions for non-diamond and diamond deposition are now properly located in the corresponding regions of the in-situ ternary diagram. The experimental conditions, which resulted in no carbon deposition from the vapor phase, remained within the diamond-growing region. Fig. 5 shows the location of their data and the resulting regions in the in-situ diagram. Their process conditions were modeled closely with a temperature of 900°C (1173 K) and pressure of 50 torr.

The mole fraction of CO in Marinelli's no-growth experimental condition is only 1% greater than that with the diamond growth condition. However, there is a 5% decrease in the mole fraction of CO between experimental conditions that resulted in non-diamond and diamond growth. Such a decrease in the mole fraction of CO allows for a much greater carbon concentration to remain within other participating species. So, while CO is assumed not to be instrumental in diamond deposition, it does influence the gas-phase chemistry and composition. The reason for the observed non-resolvability of Marinelli's no-growth experiment using the new C–H–O ternary diagram is not clear. Typically, there is more uncertainty associated with the experimental observations of no-carbon precipitation than that with non-diamond carbon precipitation.

The pressure effect on the new C–H–O ternary diagram was also studied. Typically, the experimental limits for diamond deposition from the vapor phase is wide (mtorr — hundreds of torr) compared with temperature limits. The analysis of the results at different pressures (5 torr, 50 torr and 200 torr) indicates that pressure changes the boundaries of the radical species compositional domain for diamond deposition. The diamond domain widens with decreasing pressure as shown in Fig. 6. Also, the atomic hydrogen concentration increases with decreased pressure thus locating the points on the triangular diagram closer to the hydrogen vertex. In contrast, Fig. 7 shows that at 200 torr, the diamond domain has narrowed to such an extent that boundary lines can no longer be confidently drawn. This is an interesting observation in that the results indicate that it is easier to obtain non-diamond deposition at higher pressures than at lower pressures.

The results shown in Fig. 7 reflect the effect of

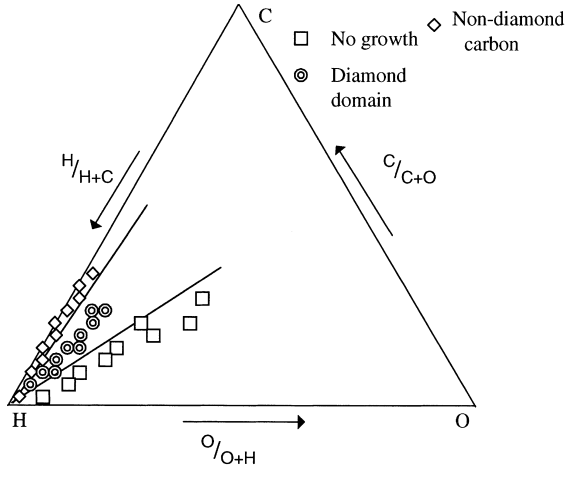

Fig. 6. Resulting C–H–O ternary phase diagram based on radical species composition at 5 torr pressure and 1150 K.

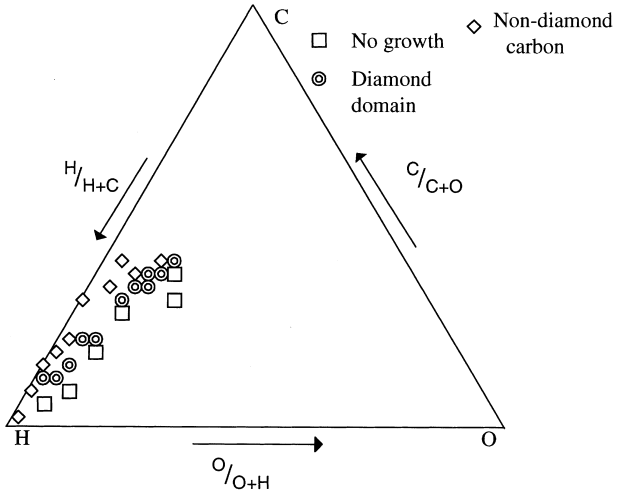

Fig. 7. Resulting C–H–O ternary phase diagram based on radical species composition at 200 torr and 1150 K.

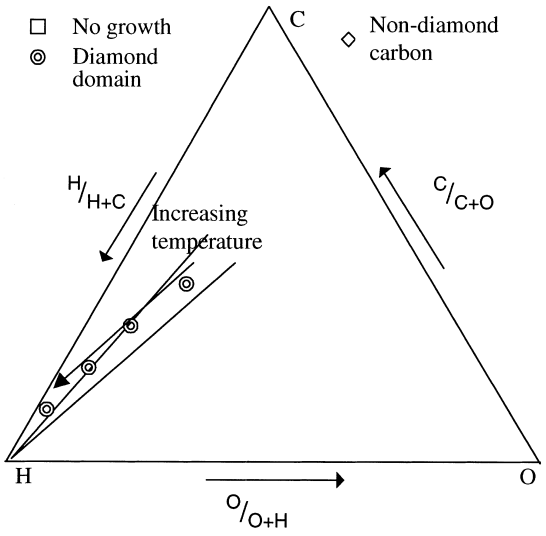

Fig. 8. Resulting radical species composition with increasing temperature starting from 1150 K at 100 K intervals at 50 torr pressure plotted on the C–H–O phase diagram shown in Fig. 2.

pressure for reactors operating with modest microwave power conditions, i.e. 500–1500 W. In the model, the bulk gas phase and the growth interface were at same temperature. The computations presented in this paper do not directly apply when the bulk gas phase attains temperatures much higher than 1150 K. The bulk gas phase temperature could be as high as 5000 K at higher power densities ($\sim$ 5 kW) and at high pressures ($\sim$ 200 torr) [1]. At bulk gas phase temperatures $\gg$ 1150 K, the steady state gas phase composition would resemble closely that of equilibrium composition at that temperature [14] and that will increase the overall portion of the participating species at the growth interface. At normal process conditions (MW of 0.5–1.5 kW), the portion of participating species decrease with increasing pressure as shown in Table 2. The main effect of an increase in pressure and microwave power is on the bulk gas phase temperature and composition. Because of this, the overall portion of radical species close to the growth surface would increase and possibly contribute to widening the diamond deposition domain in the new in-situ diagram. For studying the effect of microwave power density and pressure on the new in-situ diagram, one should include a one-dimensional model allowing for mass transfer along with the steady state computations for gas phase and gas-surface chemistry. This will be a subject of our future communication.

If the substrate temperature is too high, then the non-diamond carbon deposition will result even if the feed conditions are located within Bachmann's diamond growing domain. Since temperature affects the relative concentrations of the participating species, such a temperature effect is expected to show up in the in-situ C–H–O diagram. Fig. 8 clearly indicates that at constant feed composition, the participating species composition migrate from the diamond growing domain to the non-diamond carbon domain when temperature increases beyond 1400 K.

Table 2
Effect of pressure on steady-state fractions of gas phase composition[a]

	5 torr	15 torr	50 torr	200 torr
Participating species	0.4406	0.2005	0.0653	0.0248
H	0.4338	0.196	5.74×10^{-2}	1.09×10^{-2}
Non-participating species	0.5594	0.7995	0.9347	0.9752
CO	0.1105	0.1305	0.135	0.1283
H_2	0.4425	0.662	0.7883	0.8248

[a] Temperature is 1150 K. Feed conditions are 20% methane, 10% oxygen, and 70% hydrogen.

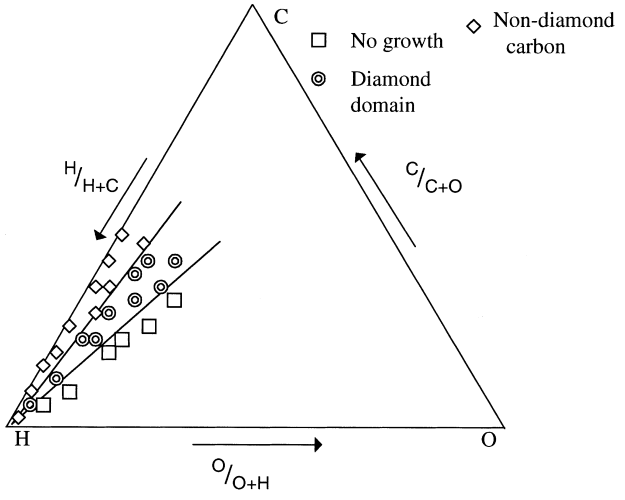

Fig. 9. The resulting C–H–O ternary phase diagram based on radical species composition when computed at flow rate of 400 sccm. Pressure was 50 torr and temperature was 1150K.

Fig. 9 shows the effect of decreasing the residence time from 10 to 5 s. The boundaries of the different regions are slightly shifted towards the carbon vertex with increase in flow rate while narrowing the diamond domain. These results on the effect of flow rate on the new C–H–O diagram is probably less accurate than that with pressure and temperature because the model does not account for any transport effects.

The in-situ C–H–O diagram (Fig. 2) would be useful in explaining various experimental observations with radical species-morphology interactions. In addition, such a diagram should find applications in the scale-up, deposition onto complicated geometries such as trenches, and on the quality of resulting diamond films on a macro scale. In fact, the in-situ diagram in Fig. 2 was used successfully for modeling the effect of oxygen on diamond deposition inside micro-trenches [15]. The Bachmann diagram based on feed gas composition would not provide any useful information on the effect of oxygen on a diamond deposition at a particular aspect ratio of a trench.

4. Summary

A new in-situ C–H–O ternary phase diagram for diamond deposition from the vapor phase is constructed based on radical species composition. This construction is based on a zero-dimensional, steady-state computations of gas phase and gas-surface chemistry for data points presented in the Bachmann diagram based on feed gas compositions. The analysis further indicates that CO species, although dominating in composition, may not participate in the surface chemistry during diamond growth and had to be treated as non-participatory. The following observations are made on the new in-situ C–H–O ternary phase diagram based on radical species composition:

- It distinguishes the contradicting experiments using methane and carbon dioxide as feed gases by Marinelli et al. [3] for non-diamond deposition and diamond deposition.
- It also distinguishes the effect of temperature on diamond deposition.
- The effect of pressure on the in-situ C–H–O ternary for reactors operating at modest microwave power shows that the diamond deposition domain shrinks with increasing pressure. Due to zero dimensional nature of the computations, the effect of combination of variables such as microwave power density and pressure on the in-situ C–H–O diagram is not determined.

Acknowledgements

The authors gratefully acknowledge the financial support from NSF through a CAREER award (# CTS 9876251) and from the KY state EPSCoR program through KSGC fellowship (S.E.) and from the University of Louisville through an Undergraduate Research Grant. The authors acknowledge Professor John C. Angus of Case Western Reserve and the reviewer for their helpful comments.

References

[1] P.K. Bachmann, D. Leers, H. Lydtin, Diamond Relat. Mater. 1 (1991) 1.
[2] P.K. Bachmann, H.-J. Hagemann, H. Lade et al., MRS Proc. 339 (1994) 267.
[3] M. Marinelli, E. Milani, M. Montuori et al., J. Appl. Phys. 76 (1994) 5702.
[4] N.A. Prijaya, J.C. Angus, P.K. Bachmann, Diamond Relat. Mater. 3 (1993) 129.
[5] J. Wang, Y. Wan, Z. Liu, H. Wang, D.W. Zhang, Z. Huang, Mater. Lett. 33 (1998) 311.
[6] National Institute of Standards and Technology. http://www.nist.gov/cstl/div836/ckmech/ReactionData.html
[7] S.J. Harris, A.M. Weiner, J. Appl. Phys. 67 (1990) 6520.
[8] C.C. Battaile, D.J. Srolovitz, J.E. Butler, J. Appl. Phys. 82 (1997) 6293.
[9] R.S. Sinkovits, C.R. DeVore, V.A. Shamamian, Diamond Relat. Mater. 5 (1996) 1344.
[10] S.J. Harris, Appl. Phys. Lett. 56 (1990) 2298.
[11] J. Harris, A.M. Weiner, J. Appl. Sci. 74 (1993) 1022.
[12] J.E. Butler, R.L. Woodin, in: A. Lettington, J.W. Steeds (Eds.), Thin Film Diamond, Chapman and Hall, London, 1994, p. 15.
[13] W.D. Cassidy, E.A. Evans, Y. Wang et al., MRS Proc. 339 (1994) 285.
[14] P.K. Bachmann, The physics of diamond, in: A. Paoletti, A. Tucciarone (Eds.), Proceedings of the International School of Physics, Course CXXXV, IOS Press, Amsterdam, 1997, p. 45.
[15] S.C. Eaton, M.K. Sunkara, M. Ueno, K. Walsh. Diamond Relat. Mater. (1999) submitted.